Acquisition of Crosswell Seismic Monitoring Data

Thomas M. Daley[1], Fenglin Niu[2], Paul G. Silver[3], and Ernest L. Majer[1]

[1]Lawrence Berkeley National Laboratory, [2]Rice University, [3] Carnegie Institute

Abstract

Crosswell seismic acquisition provides an ideal geometry for monitoring travel time changes in the subsurface. Analysis of delay time in terms of a characteristic frequency allows us to estimate optimal acquisition parameters (frequency and distance). We have deployed standard data acquisition equipment for continuous monitoring of crosswell travel time in two separate field experiments, with well spacing of 3 and 30 m. The acquisition hardware used for the field experiments is described, along with environmental effects (such as temperature) that influence the measurements. Two field experiments are described that correlate changes in travel time (and therefore velocity) with changes in barometric pressure. The results from the two field sites show a pressure sensitivity for velocity of 10^{-6}/Pa to 10^{-8}/Pa.

Introduction

Seismic velocity (both compressional and shear) is a fundamental property of materials, one that varies with changes in conditions both external (stress, temperature) and internal (fluid saturation, crack density). Monitoring of changes in these external or internal conditions is a goal of geophysical investigations such as earthquake prediction (via stress change monitoring) and reservoir exploitation (via fluid saturation monitoring). The simplest means of observing a time-dependent stress change, using an active source and fixed receivers, is to measure the delay time between subsequent source pulses for the same path. The precision at which this measurement can be made determines the precision to which stress changes can be detected, and the interval between measurements determines the temporal resolution. Active-source, continuous monitoring of seismic velocity can provide high-precision *in situ* measurement of temporal changes. Using a crosswell geometry for acquisition (i.e., having source and sensors, at depth, in separate boreholes) provides a methodology for spatially localizing the monitored region. Ideally, the source and sensors would both be in a formation of interest, and only changes in that formation will affect the data. This minimizes the effects of near-surface changes, which are often unwanted "noise," and simplifies data analysis.

An important component of *in situ* monitoring with active-source seismic measurement is

calibrating the change in seismic P- or S-wave velocity with a known stress variation, such as earth tides or atmospheric pressure change. This calibration would allow the identification of those parts of seismic velocity changes that are caused by stress change in a given rock volume, and allow an *in situ* determination of the stress-velocity relationship. Changes in seismic velocity induced by solid-earth tidal loading and variations in barometric pressure have been estimated in some studies. The fractional change in seismic velocity with respect to stress change (i.e., the pressure sensitivity) is reported to be in the range of 10^{-9}/Pa to 10^{-6}/Pa (De Fazio et al., 1973; Yukutake et al., 1988; Sano et al., 1999).

Previous active source monitoring efforts had variable resolution of *in situ* velocity changes; however, recent work has shown dramatic improvement. The major advances, compared to the earlier studies, are twofold. First, the characteristics of available seismic sources have significantly improved, primarily in repeatability. Detection of travel-time changes is maximized for highly repeatable sources that can operate at high frequency and for extended periods of time. Previous work used sources, such as surface vibrators or air guns, that were difficult to keep running for extended periods and had limited repeatability. Modern piezoelectric borehole sources are highly repeatable and dependable for millions of source excitations. Second, the precision in measuring differential travel time has increased, made possible in large part by the greatly increased sample rates available with modern high-speed data acquisition systems using high speed internal clocks, and by the computational capability of performing massive waveform stacking. Additionally, the development of seismic sensors, both coil/magnet type geophones and piezoelectric-type hydrophones, has improved sensitivity and dependability over recent decades. Studies with permanent installations have demonstrated the improvement in monitoring resolution.

A logical next step is to take this continuous monitoring measurement capability to field sites and use equipment designed for temporary deployment in wells of opportunity, allowing *in situ* monitoring to assess the sensitivity of a given site and then redeployment when and if desired. In this paper, we present techniques used for *in situ* travel-time monitoring using shallow (10–100 m) field site boreholes, with equipment designed for crosswell seismic acquisition, recorded for

time periods of 6 and 35 days at two separate sites. The analysis is focused on correlation of barometric pressure changes to velocity changes, allowing calibration of the stress sensitivity.

Optimal Acquisition Parameters

For a given acquisition geometry, we would like to optimize acquisition parameters such as frequency content and source-receiver distance, which tend to scale (i.e., lower frequencies at larger distances due to attenuation). In travel-time monitoring, we measure, τ , the lag time between an arriving wavelet (usually the first) on two seismograms, with a total travel time *T*, and a center or characteristic frequency f_0. If we express both τ and *T* in terms of the characteristic frequency, f_0, $\tau = \varepsilon / f_0$, $T = N / f_0$, where *N* is the number of wavelengths between the source and receiver and ε is a normalized time delay. Then the velocity perturbation, $\delta\hat{v} = \delta V/V$, can be simply rewritten as the ratio of two dimensionless parameters:

$$\delta\hat{v} = \varepsilon / N. \qquad (1)$$

This particular parameterization provides a simple way of scaling experiments both in terms of frequency and spatial extent. From Equation (1), it is clear that achieving the lowest possible detection threshold for $\delta\hat{v}$ can be broken into two separate tasks: (1) maximizing the number *N* of wavelengths between source and receiver, and (2) increasing the precision in measuring normalized delay time, ε (effectively the phase). The first task, maximizing *N*, is a property of the medium, the geometry, and the source characteristics, since *N* can be written as $N = Lf_0/V$. Thus, the acquisition geometry (path length) and maximum frequency (which is a function of source output and the medium's attenuation), will factor into determining *N*. The second task is a function of frequency content and signal-to-noise. The attenuation, Q, will affect the signal-to-noise and therefore the precision. It can be shown that the optimal $N \sim Q/\pi$.

For Q = 60, a typical upper crust value, we have N~20, and assuming the P velocity is 1.5 km/s, the optimal frequencies for source-receiver distances of 3 m, 30 m, 100 m and 1000 m (corresponding to the distance range that we expect to encounter) are 10 KHz, 1.0 KHz, 330 Hz, and 33 Hz, respectively. To the extent possible, we use the optimal frequency in the data acquisition design. For our two test sites, we were able to use 10 kHz and 1 kHz at 3 and 30 m,

respectively.

Acquisition Hardware

Data acquisition for continuous crosswell monitoring builds on development of crosswell seismic work of the previous 10–20 years, which was usually designed for tomographic imaging (e.g., Daley et al., 2004; Majer et al., 1997, Rector, 1995) but more recently has been used for time-lapse monitoring (e.g., Vasco, 2004; Hoversten et al., 2003). Three major data acquisition components are involved: seismic source, seismic sensor, and the recording system. (Our acquisition was conducted with a combination of commercial and specially built equipment—the piezoelectric source and the high voltage amplifier used to power it.). The source is cylindrical rings of piezoelectric ceramic (lead zirconate titanate) epoxied together and wired for positive and negative voltage on the inner and outer surfaces. This type of source has been used in many seismic crosswell surveys (e.g., Majer et al., 1997; Daley et al., 2004) and is known to be repeatable and dependable. The tests reported here used a single-cycle square wave generated by a source waveform generator (in this case, a programmable analog signal generator), which also sends a trigger signal to the recording system. Other source waveforms are known to provide greater signal-to-noise ratio. The sensors were commercial hydrophones designed for large bandwidth and high sensitivity, using piezoelectric film and built-in amplifiers with analog data transmission to the surface recording system.

The commercial recording system, a “Geode” manufactured by Geometrics, has a 24 bit analog-to-digital converter using a sigma-delta conversion algorithm. Our data was collected at a sampling rate of 48,000 samples per second. The triggering of the recording system for each shot is an important consideration. The digitizer, continually sampling the data, receives a trigger that will generally be between two digitized samples. Including a section of pre-trigger data, the time series is interpolated and resampled, so that the time series begins at the time of the trigger. This start time is not exact, and at a sampling rate of 48,000/s, this time is computed to within $1/20^{th}$ of a sample (Geometrics engineering, personal communication). Thus, there is a delay time measurement error that will be $1/40^{th}$ of a sample (half-way between samples), and the average error will be an $1/80^{th}$ of a sample, assuming that errors are uniformly distributed—

corresponding to an average error of 260 ns per trigger. The error in the stacked data is smaller by a factor of $N^{1/2}$, assuming they are uncorrelated. For N=36,000 traces, as in the case of our experiments, the error is thus 1.4 ns for 1 hr sampling, which is below other sources of error.

Field Tests

Our first test was conducted at a distance of about 3 m between two 15 m deep holes at Lawrence Berkeley National Laboratory (LBNL). The piezoelectric source was placed at the bottom of one hole. The source power supply for this test was a commercial high-voltage pulser, made by Cober Electronics. The sensor cable had 24 sensors at 0.5 m spacing, spanning most of the second hole. All 24 sensors were recorded. The source was pulsed every 100 ms with a record length of 10 ms, which yields 10 traces per sensor per second. These individual traces were stacked in the acquisition system, with a stacked set of 24 traces output every minute. A one-minute record is thus a stacked recording consisting of a real-time stack of 600 single traces for each sensor. An example of a single shot record (no stacking) for all 24 sensors is shown in Figure 1. The signal-to-noise ratio is very high even without any stacking, especially for those sensors in the middle of the receiver string. The sensors near the surface (channels 18–24) had much lower signal level because they were above the water table in a much more attenuative medium. One advantage of using multiple receivers is that we can select channels to be analyzed in order to obtain an ε value as low as possible.

In this 3 m experiment, we continuously recorded a total of 160 hours, starting from November 12, 2003. The SNRs average was ~4000 for the stacked one-minute records. Figure 2a shows that the SNR for this experiment continues to increase for up to 10^4 stacks, implying that a nonrandom noise "floor" has not been reached. Figure 2b shows the histogram of the measured delay time between two adjacent one-minute records, which follows a normal distribution with a standard deviation of ~50 ns. Since the P-wave velocity at the test site is ~1.5 km/s, the travel time, T, is ~2 ms. For one-hour stacked records, we can achieve a standard deviation, or precision, of up to 6 ns, which corresponds to a resolution of 3×10^{-6} for the velocity perturbation, $\delta\hat{v}$. Our actual precision is possibly better than this, since there is a contribution from actual stress-induced velocity perturbations in the histogram. This nanosecond precision is the key to

successful stress monitoring.

In this experiment, we measured the delay time using two different time windows: a short time window, which includes the first arrival only (1.4 cycles), and a long time window, which contains both the first arrival and coda (10 cycles). The measured delay times with respect to the trace using the two time windows are plotted in Figures 3a and 3b. Both show a time variation of ~3 μs (for a travel time of ~2 ms), corresponding to $\delta\hat{v}$ of 10^{-3}. We also show the variations in barometric pressure (Figure 3c) and dilatation (Figure 3d) recorded by a nearby strainmeter. During the period of observation, we see a large pressure excursion (~10^3 Pa), which continues for 3 days (Figure 3c). The delay times closely track this barometric pressure change. Using the variations in delay time and the barometric pressure change, we obtain a value for stress sensitivity of ~10^{-6} /Pa. Cross correlations between delay time with barometric pressure look very similar to the autocorrelation of the delay time with itself, demonstrating that, at least over long periods, there is an excellent correlation (Figure 3e-g).

The sign of the travel time fluctuation relative to the barometric pressure (increasing travel time for increasing pressure) is the opposite of standard expectation and requires some explanation. An increase in barometric pressure acting directly on the borehole will raise pore pressure and decrease effective stress in the near-field region next to the borehole. In the far field, the same increase in barometric pressure will act on unchanged pore pressure and increase the effective stress. The change in seismic velocity along a particular ray path thus depends on the net change in effective stress. When two boreholes are relatively close, near-field effective stress can decrease and cause a decrease of seismic velocity.

After the LBNL site work, we wanted to deploy in deeper wells and at a longer interwell distance, hopefully moving out of the near-well conditions at the LBNL site. We chose to deploy in wells at the Richmond (California) Field Station (RFS), a test site on San Francisco Bay near the University of California, Berkeley. The RFS test site has several boreholes approximately 70 m deep and 30 m apart from each other (Daley and Gritto, 2001). After initial testing in 2004 to choose and stabilize the acquisition equipment, the final monitoring was performed in early

2005, (Jan 31 to March 23). A 4-inch piezoelectric source was set in well EMNE 25 m below surface, and the 24-element hydrophone array was placed in EMNW at the depth range 25–36.5 m below surface. The source high-voltage amplifier was custom made using IGBT (Integrated Gate Bipolar Transistor) technology. The high-voltage amplifier is designed to provide power for short-duration pulses to capacitive loads such as the piezoelectric ceramic. The source amplifier is broadband (500 Hz to over 10,000 Hz) and the input is an arbitrary waveform. A schematic of the acquisition system used at RFS is shown in Figure 4. At RFS, the source waveform was a 1 ms wide pulse (half cycle of a square wave), and the output waveform had 1.2 kV peak-to-peak amplitude. The source was repeated 10 times per second, with a 50 ms record length, and these pulses were stacked by the recording system to give recordings every 1 minute (600 pulses). For this study, we attempted to reduce any movement of the sensors with "centralizers" (flexible bands of metal acting like springs), which kept 3 of the sensors fixed, and with hard foam attached to the source. Figure 5 shows the sensors with centralizers and the source with foam. Unfortunately, at some point during deployment, the source foam was compressed, apparently by the water pressure.

The dominant frequency observed in the RFS data was about 1 kHz; travel time was about 20 ms (a Vp of 1.5 km/s). Compared to the LBNL test, the data frequency is about 1/10, but the travel time is 10 times as large, such that we achieve a resolution for $\delta\hat{v}$ that is essentially the same as the value we obtained at LBNL, $\sim 3\times10^{-6}$.) The signal-to-noise ratio of 1-minute stacks is 604 with a standard deviation of 39.2 ns, while 1-hour stacks have a SNR of 3185 with 5.2 ns standard deviation. We recorded 35 days of continuous data in the RFS test.

The RFS data, shown in Figure 6a, required some initial preprocessing. Bad shots were deleted and the long-term trend was removed. The cause of the long-term trend is not known, but it has a period longer than our signals of interest. During the 30 m experiment, we found that ambient surface temperature (Figure 6b) had a measurable effect on the data, and we observed that delay time correlates very strongly with temperature. The recording of temperature inside the recording container allowed correction for temperature variation. Scaling is about 0.1 □s/ºC, as shown in Figure 6d, where swings of 10ºC correspond to oscillations in delay time of about a microsecond.

This is a large error, which we have treated in two ways. First, we can solve for a temperature correction coefficient and subtract out this effect, assuming it is linear; we estimated a linear scaling constant between the measured temperature and the delay time variation. The scaled temperature data was then subtracted from the delay time data. This was effective in minimizing the 24-hour variation in delay time due to temperature. Second, we can minimize the effect by maintaining the electronics within a temperature range, achieved midway through the experiment by installing thermostat-controlled heating and air conditioning in the recording container, which stabilized the temperature. The temperature control began on Day 17, and the minimimization of temperature variation can be seen in Figure 6b. We were successful in maintaining temperature variation within ~2^{o}C using standard commercial thermostats to control heating and cooling.

The data collection period included a time of heavy rain, and we found that the correlation to barometric pressure had changed following this rainfall event, making the data from the rainfall period problematic to interpret. At least two possible effects are involved: an increase in surface load (increasing effective stress) caused by the mass of the rain water, and an increase in pore pressure (decreasing effective stress), caused by the infiltration of rain water. The effect on travel time due to rain is therefore difficult to interpret, and we make no such attempt. Figure 7 shows the delay time and barometric pressure for two time periods, before and after the rain, corresponding to Days 1–14 and 24–36. In the first time period, a delay time change of 1 ms approximately corresponds to a barometric pressure change of 15 millibar, giving a stress sensitivity of about 5×10^{-8} /Pa. The second time period had a stress sensitivity of about 12.5×10^{-8} /Pa. Importantly, the sign of travel-time fluctuation relative to the barometric pressure is now the expected decrease in travel time for increasing pressure, indicating that we are measuring the “far field” effect away from the boreholes.

Conclusions

Modern crosswell data acquisition systems have the capability to conduct high-precision subsample delay time measurements. We have acquired two crosswell monitoring data sets over time periods of 7 days and 36 days. Large sensitivity to surface temperature in the recording instruments was observed, and corrections were applied. In the second experiment, centralizers

were used to stabilize the position of the source and sensors. In these two separate experiments, we demonstrated travel-time measurement precision on the order of 10^{-7} to 10^{-8} s. This precision allows us to monitor barometric pressure as a calibration signal to measure the stress sensitivity of velocity at each field site. Near-field effects dominated our first test at 3 m spacing between wells. These effects caused the velocity to decrease with increasing pressure, with a sensitivity of 10^{-6}/Pa. In a larger-scale 30 m experiment, the velocity was observed to increase with increasing barometric pressure, with a sensitivity of 5-12.5 $\times$ 10^{-8} /Pa.

Acknowledgement

The authors would like to thank Rob Trautz of LBNL for supplying the barometric pressure logger and helping with field work. This work was supported by NSF Grants EAR-0352134 (FN), EAR-0453471(FN) , EAR-0352119 (PGS) and EAR-0453638 (PGS), Rice University, Carnegie Institution of Washington and Lawrence Berkeley National Laboratory of the U.S. Department of Energy under Contract No. DE-AC02-05CH11231.

References

Daley, T.M., E.L. Majer, and J.E. Peterson (2004), Crosswell seismic imaging in a contaminated basalt aquifer, *Geophysics,* **69**, 16–24.

Daley, T.M. and R. Gritto (2001), Field test of INEEL tube-wave suppressor and LBNL borehole seismic system at Richmond Field Station, *LBNL-49015*, Lawrence Berkeley National Laboratory Report.

De Fazio, T.L., K. Aki, and J. Alba (1973), Solid earth tide and observed change in the in situ seismic velocity, *J. Geophys. Res.,* **78**, 1319–1322.

Hoversten, G.M., R. Gritto, J. Washbourne, and T. Daley (2003), Pressure and fluid saturation prediction in a multicomponent reservoir using combined seismic and electromagnetic imaging, *Geophysics,* **68**, 1580–1591.

Majer, E.L., J.E. Peterson, T.M. Daley, B. Kaelin, L. Myer, J. Queen, P. D'Onfro, and W. Rizer (1997), Fracture detection using crosswell and single well surveys, *Geophysics,* **62**, 495–504.

Rector III, J.W. (1995). Crosswell methods: Where are we, where are we going? *Geophysics,* **60**, 629–630.

Sano, O., K. Hieda, K. Hirano, T. Hirano, H. Ishii, Y. Hirata, S. Matsumoto, and T. Yamauchi (1999), Stress-sensitivity of the sound velocity at Kamaishi mine, Paper Presented at Seismological Society of Japan 1999 Fall Meeting, Sendai, Japan.

Toksoz, M.N., and D.H. Johnston, ed. (1981), Seismic Wave Attenuation, Geophysics reprint series No. 2, Society of Exploration Geophysicists.

Vasco, D.W. (2004), Seismic imaging of reservoir flow properties: Time-lapse pressure changes, *Geophysics*, **69**, 511–521.

Yukutake, H., T. Nakajima, and K. Doi (1988), *In situ* measurements of elastic wave velocity in a mine, and the effects of water and stress on their variation, *Tectonophysics*, **149,** 165–175.

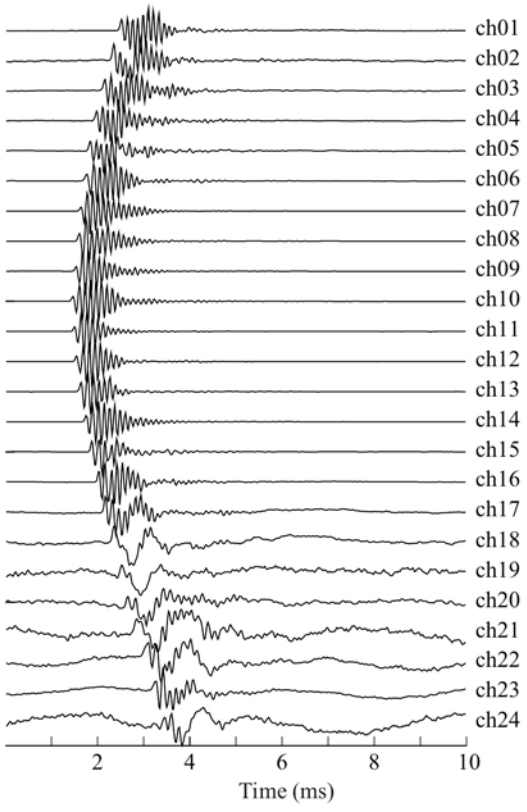

Figure 1. A single recording (no stacking) for the 24 sensors at 0.25 m spacing from the LBNL data set. The well spacing is 3 m. The dominant frequency is about 10,000 Hz.

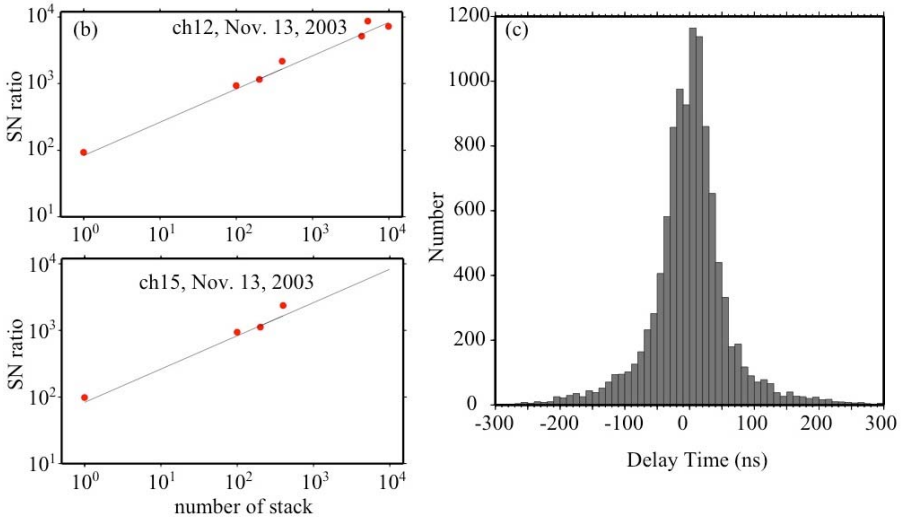

Figure 2. (a) (left) The increase in signal-to-noise ratio versus the number of stacked recordings for two data channels (ch12 and ch15 from Figure 1); (b) (right) A histogram of the delay time measurements between adjacent one-minute stacks (600 records) with a standard deviation of about 50 ns (10^{-9} s).

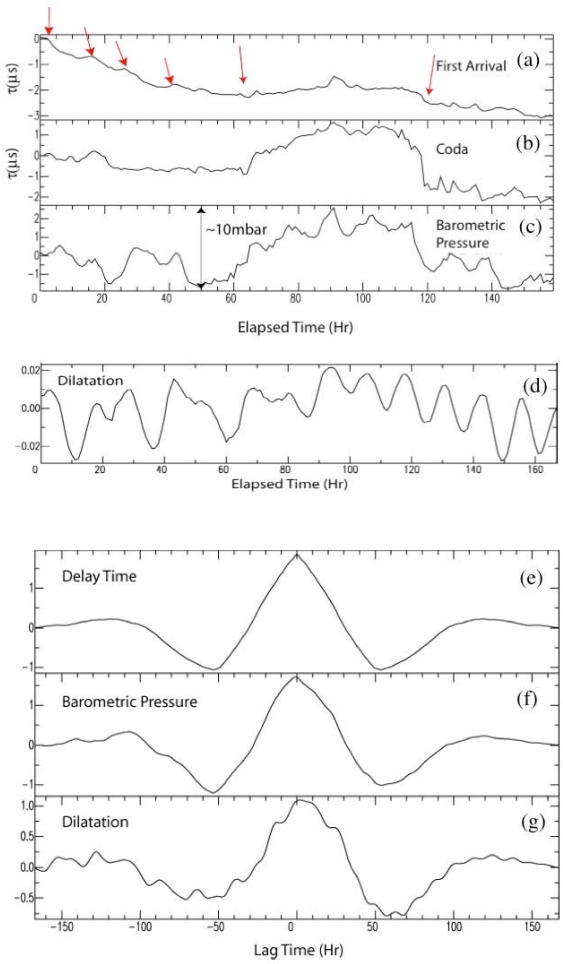

Figure 3. (a) Delay time measured from first arrival time window; (b) Delay time measured from window with 10 cycles of coda; (c) Barometric pressure measured at surface; (d) Dilation measured from near region strain meter; (e) Auto correlation of delay time; (f) Cross correlation of delay time and barometric pressure; (g) Cross correlation of delay time with dilation.

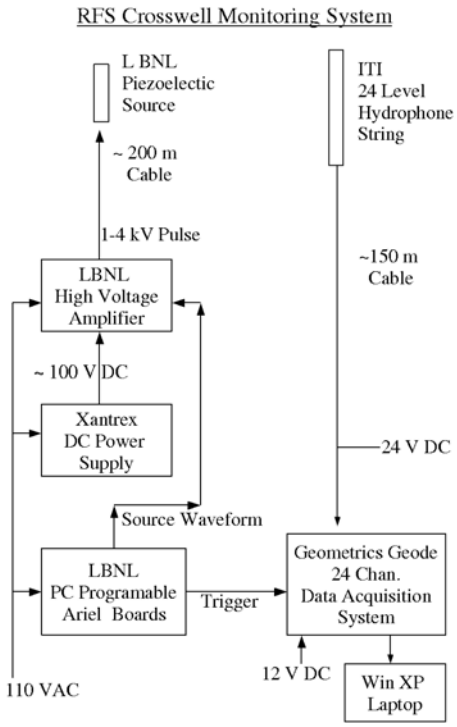

Figure 4. Schematic of data acquisition equipment used in the 36-day monitoring experiment at RFS.

Figure 5. (left) Seismic sensor (hydrophone) with centralizer as used at RFS experiment; (right)

Piezoelectric seismic source with foam centralizer, as used at the RFS experiment.

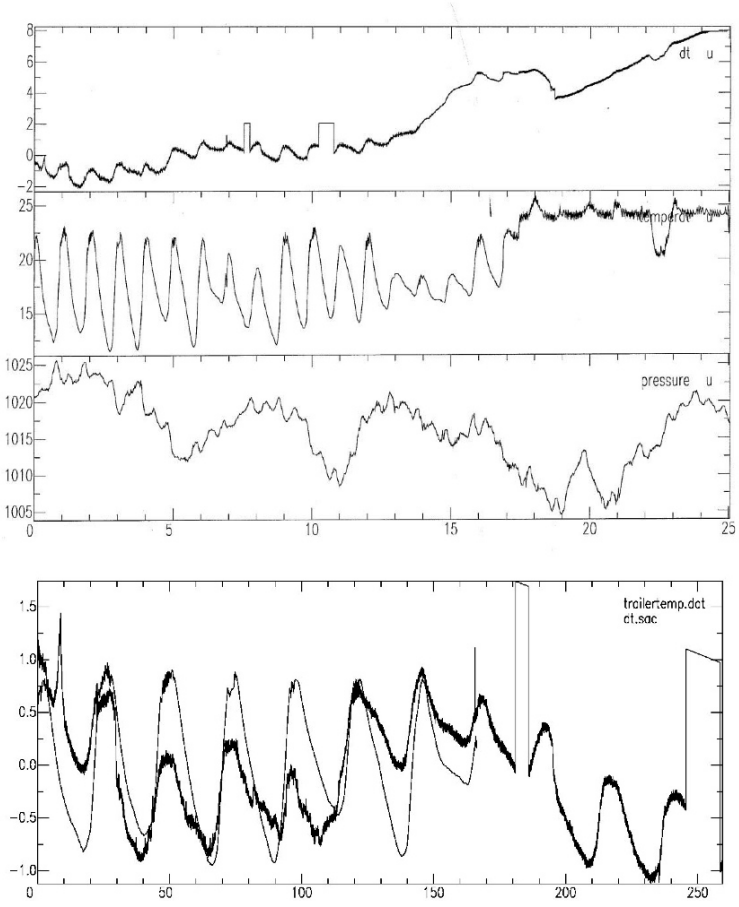

Figure 6. (a) (top) Measured raw delay time for the RFS experiment for first 25 days—excursion from 14 to 20 days is during heavy rainfall; (b) Measured temperature inside the recording container; (c) Measured barometric pressure; (d) (bottom) Comparison of raw delay time and temperature for initial 250 hours at RFS.

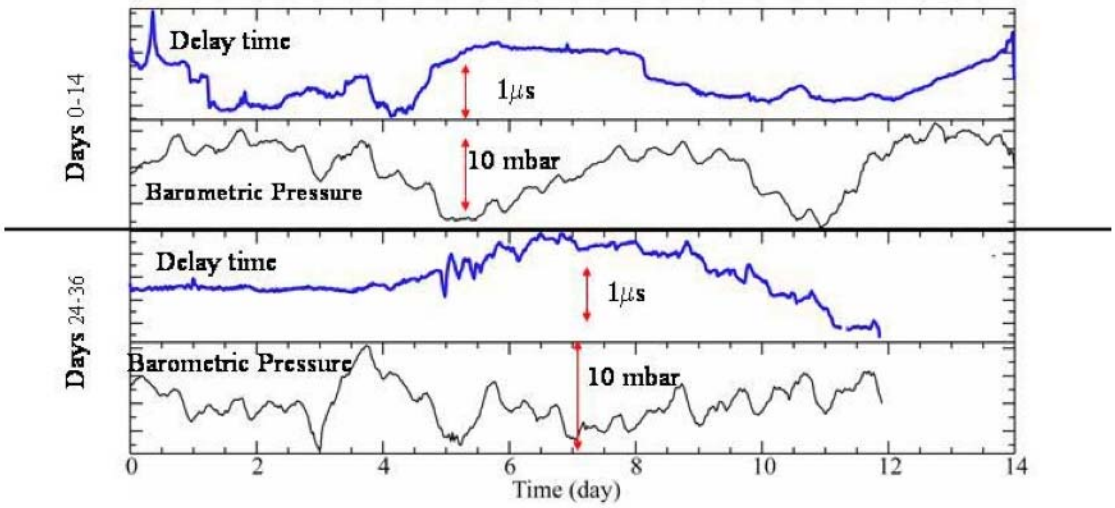

Figure 7. Delay times after temperature correction and removal of the linear trend from the data in Figure 6a are shown with barometric data for Days 1–13 (top) and 24–36 (bottom).